

# Direct Observation of Ultracold Bimolecular Reactions

M.-G. Hu,<sup>1,2,3,\*</sup> Y. Liu,<sup>2,1,3,\*</sup> D. D. Grimes,<sup>1,2,3</sup> Y.-W. Lin,<sup>1,2,3</sup>

A. H. Gheorghe,<sup>2</sup> R. Vexiau,<sup>4</sup> N. Boulufa-Maafa,<sup>4</sup> O. Dulieu,<sup>4</sup> and K.-K. Ni<sup>1,2,3,†</sup>

<sup>1</sup>*Department of Chemistry and Chemical Biology,*

*Harvard University, Cambridge, Massachusetts, 02138, USA.*

<sup>2</sup>*Department of Physics, Harvard University, Cambridge, Massachusetts, 02138, USA.*

<sup>3</sup>*Harvard-MIT Center for Ultracold Atoms, Cambridge, Massachusetts, 02138, USA.*

<sup>4</sup>*Laboratoire Aimé Cotton, CNRS, Université Paris-Sud,*

*ENS Paris-Saclay, Université Paris-Saclay, 9145 Orsay cedex, France*

(Dated: May 27, 2022)

Chemical reactions result in the conversion of reactants to products through an intermediate state or a transition state. Unambiguous identifications of and investigations of chemical reactions are thus most complete when detecting all of the involved relevant species: reactants, products, and any transient intermediate states. Although direct observation of an intermediate collision complex is challenging because it is generally short-lived, it holds many of the key insights to understand the reaction bond breaking and forming processes. Femtochemistry techniques have been instrumental in resolving the short time scales necessary to directly probe transient intermediates for unimolecular reactions. In this work, we take the contrasting new approach of prolonging the lifetime of the intermediate by preparing reactant molecules in their lowest ro-vibronic quantum state at ultralow temperatures, thereby drastically reducing the number of exit channels accessible upon the collision of a pair of molecules. Using ionization spectroscopy and velocity-map imaging (VMI) of a trapped gas of potassium-rubidium molecules at a temperature of 500 nK, we directly observe reactants, intermediates, and products of the four-center reaction  $^{40}\text{K}^{87}\text{Rb} + ^{40}\text{K}^{87}\text{Rb} \rightarrow \text{K}_2\text{Rb}_2^* \rightarrow \text{K}_2 + \text{Rb}_2$ . This work reveals a long-lived energy-rich intermediate complex and opens the door for studies of quantum-state resolved reaction dynamics in the ultracold regime.

---

\* These two authors contributed equally.

† To whom correspondence should be addressed. E-mail: ni@chemistry.harvard.edu

The creation of ensembles of molecules at ultralow temperatures opens a new era of fundamental chemical reaction studies, one where the slow motion of the molecules exemplifies the role of quantum mechanics. Ultralow temperatures enable high resolution spectroscopic studies, allow opportunities for the broader exploration of reaction phase space, and grant the promise of eventually gaining control over the outcome of chemical reactions. Already, investigations of single partial wave collisions take the usual place of spectroscopy to provide detailed benchmarks of short range molecular potentials [1, 2], exotic conditions at low temperatures facilitate the synthesis of new chemical species [3], and highly sensitive and precise methods of detection make possible studies of state-to-state reactions between atoms and weakly-bound Feshbach molecules [4]. Further, chemical reaction rates for barrierless reactions can be altered [5, 6], in some case by orders of magnitude, merely by changing the nuclear spins of the reactants and through Pauli blocking effects at quantum degeneracy [7]. These studies all rely on unprecedented levels of control over the quantum state of ultracold molecules, and further possibilities are abundant, including use of geometric phase and external fields to control chemical reactions [8].

Despite recent advances in ultracold molecules, a key capability has been missing: namely, the ability to follow a reaction from start to end including any reaction intermediates. Previous experiments show evidence of ultracold reactions between bi-alkali molecules through the quantum state-specific detection of loss of reactants [5], similar to that shown in the inset to Fig. 1, giving insights into how long-range forces determine the kinetic collision rates of the reactants. These reactions have been observed to occur with a high probability after even a single collision, approaching unity in certain cases [5, 9, 10]. Despite four decades of control over the precise ro-vibrational quantum state of the reactants to open up additional energetically allowed reaction channels, no significant differences based on the reactant species or initial quantum state have yet been observed [9, 10], and the nature of the molecular loss is still under debate [11].

Upon the initial approach of two molecules, an energy-rich intermediate collision complex is formed, the dynamics of which could hold the key for understanding the details of these ultracold, barrierless, bimolecular reactions. In higher-temperature reactions, this transient complex only exists for one or two vibrational periods, and at most on the order of a rotational period ( $\sim 1$  ps) [12, 13]. Studying this complex in the gas phase has typically required either ultrafast [14–17] or stabilizing collisional [18–20] techniques. Frequency-domain spectroscopic investigations of this intermediate state, on the other hand, are best suited to

provide structural information of the collisional complex [21, 22] and are less sensitive to the details of the dynamics. Direct observation of this intermediate complex would allow for a greater understanding of the overall kinetics and dynamics of a reaction. Based on the Rice-Ramsperger-Kassel-Marcus (RRKM) theory, the lifetime of the intermediate complex is given by  $\tau_c = 2\pi\rho_c/N_o$ , where  $\rho_c(E)$  denotes the density of states of the intermediate complex near the incident energy,  $E$ , and  $N_o$  is the number of energetically allowed exit channels (Fig. 1). Preparing reactants in the pure ro-vibronic ground state in the ultralow temperature regime tightly constrains the number of energetically allowed exit channels, greatly extending the lifetime of the intermediate complex. For reactions between alkali molecules, depending on the species,  $\tau_c$  has been estimated on the order of hundreds of nanoseconds to microseconds [23, 24], which makes direct observation of the complex a possible goal. However, no such observations have been made because all previous work has been based on the observation of loss of reactants. Direct multi-species detection methods are necessary in order to fully describe the details of these ultracold reactions [25].

Here, we report the direct detection of the ultracold chemical metathesis reaction  $^{40}\text{K}^{87}\text{Rb} + ^{40}\text{K}^{87}\text{Rb} \rightarrow \text{K}_2\text{Rb}_2^* \rightarrow \text{K}_2 + \text{Rb}_2$  (see Fig. 1), for which such a long-lived intermediate has been predicted [23, 24]. We combine complete quantum control over the ultracold reactants with an ionization based detection method that allows for direct and simultaneous detection of reactants (KRb), intermediates ( $\text{K}_2\text{Rb}_2^*$ ), and final products ( $\text{K}_2$ ,  $\text{Rb}_2$ ). This paves the way for studies of the chemical dynamics of ultracold reactions and opens the possibility of control over the quantum states of the products.

We begin our work by implementing the steps of Ref. [26] to create an optically trapped gas of  $v = 0$ ,  $N = 0$ ,  $X^1\Sigma^+$  ground-state KRb molecules. Here  $v$  and  $N$  are the vibrational and rotational quantum number of the molecules, respectively. In brief, ultracold K and Rb atoms are first converted to weakly-bound molecules by a magnetic field sweep (1.4 ms) through a Feshbach resonance at 546.62 G [30] with 20% efficiency. Then a pair of Raman beams are applied in a stimulated Raman adiabatic passage (STIRAP) pulse sequence (4  $\mu\text{s}$ ) to coherently transfer weakly-bound molecules into a single hyperfine state of the ro-vibronic ground state with 85% efficiency. Immediately after both the magnetic field ramp and the STIRAP pulse, we remove residual Rb and K atoms. Because the atom-to-molecule transfer is mostly coherent, we can reverse the transfer with high efficiency. To detect the ground-state KRb molecules, a reversed STIRAP sequence is applied followed by absorption imaging on an atomic transition (see example image shown in Fig. 2(a)). Typically,  $5 \times 10^3$

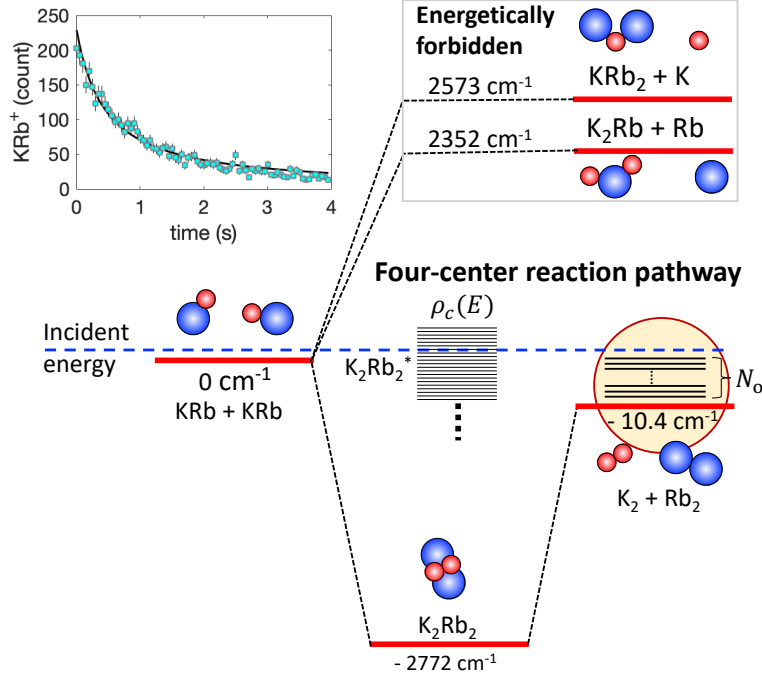


FIG. 1. **Energetics of the bimolecular reactions of ultracold KRb molecules.** The ground-state above are obtained from spectroscopy data for KRB [26],  $K_2$  [27] and  $Rb_2$  [28] and from calculation for  $KRb_2$ ,  $K_2Rb$ , and  $K_2Rb_2$  at the equilibrium configuration [29]. Here we define the incident energy of two free KRb molecules as zero energy. Because the energies of the triatomic reaction channels are much higher than that of the reactants, these channels are energetically forbidden. In comparison, the four-center reaction channel  $KRb + KRb \rightarrow K_2Rb_2^* \rightarrow K_2 + Rb_2$  is exothermic and therefore energetically allowed.  $K_2Rb_2^*$  denotes the transient intermediate complex.  $\rho_c(E)$  is the density of states of  $K_2Rb_2^*$  near the incident energy  $E$ .  $N_o$  is the number of exit channels that consist of all combinations of quantum states of  $K_2$  and  $Rb_2$  that have a total energy below  $E$ . The inset in the top-left shows the number decay of KRb molecules measured using ionization detection. The black curve is a fit to the two-body decay model used in [5].

KRb molecules are created at 500 nK with a peak density of  $10^{12} \text{ cm}^{-3}$  and are trapped by a crossed optical dipole trap (ODT) at a laser wavelength of 1064 nm.

However, because the absorption imaging detection is tied directly to the quantum state-specific STIRAP transfer, it is only sensitive to the KRb molecules in the STIRAP populated quantum state. To probe chemical reaction products and the intermediate complex, we choose a more general detection method, which is to photo-ionize neutral reaction species into bound molecular ions, accelerate the ions in an electric field, and measure their arrival time and position on a multi-channel plate (MCP) (Fig. 2(c)). By combining mass spectrometry and velocity-map imaging (VMI) [31] in our ultracold molecule apparatus, we can identify reaction species and study reaction dynamics.

We perform three separate experiments to probe the reactants, intermediate complex, and

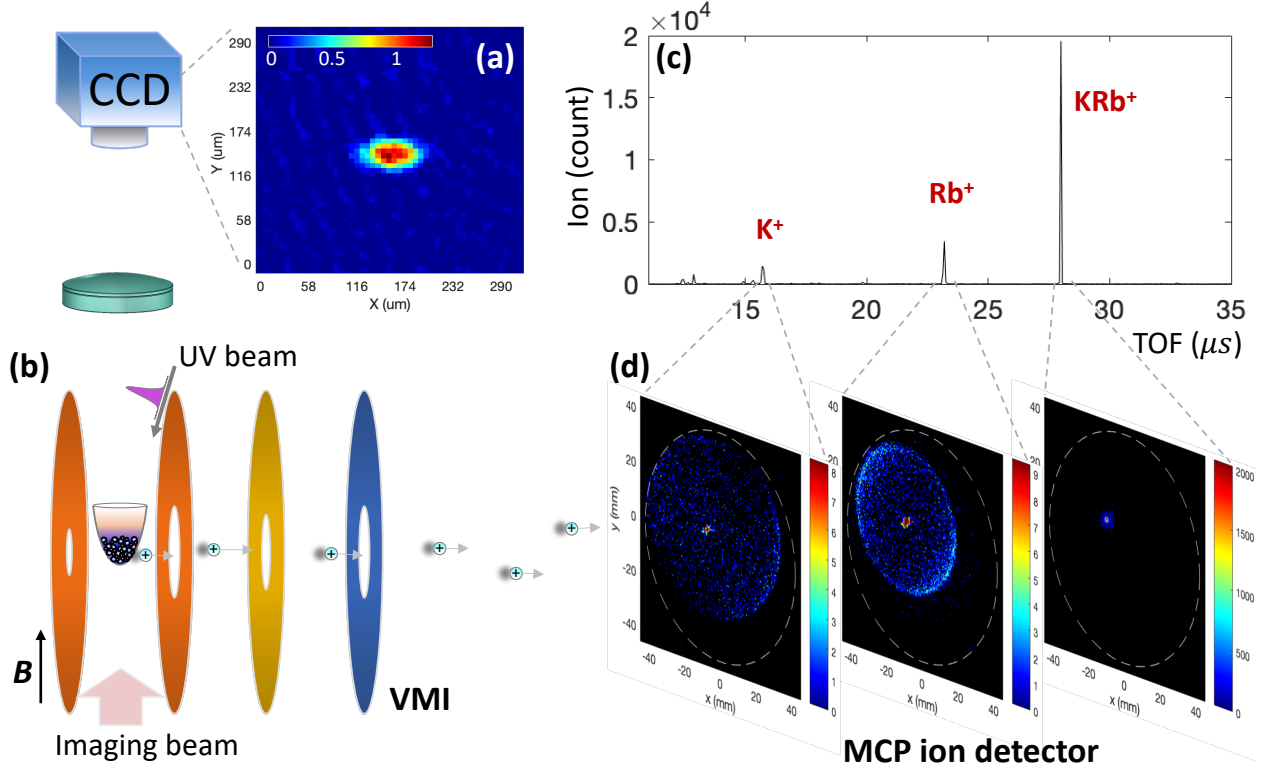


FIG. 2. **Schematic of an ultracold chemistry apparatus.** Ground-state KRb molecules at 500 nK are trapped by a crossed optical dipole trap. (a) An absorption image of KRb molecules. The colorbar indicates the optical depth of the KRb cloud. (b) These trapped molecules are surrounded by velocity-map imaging (VMI) ion optics [31], which consist of a series of disk-shaped electrodes. We use a pulsed UV laser to photo-ionize molecules. (c) An example TOF spectrum, which can be converted to a mass spectrum using the relation,  $\text{mass} = 0.16248(\text{amu}/\mu\text{s}^2) \times \text{TOF}^2$ . (d) For each species identified in the mass spectrum we also obtain a VMI image, from which its momentum distribution can be inferred.

products of the ultracold reaction. The detection procedure works as follows: After KRb creation but before the ionization pulse, we ramp the magnetic field down to 30 G within 15 ms to reduce subsequent Lorentz forces that can deflect ions away from the detector, which is housed 1 m downstream. We then apply an ultra-violet (UV) ionization pulse while simultaneously triggering the MCP to record ion signal. For the detection of reactants and products, We choose a photo-ionization wavelength of 285 nm, which is above the ionization threshold of KRb, K, Rb, as well as any species that consist of combinations of multiple K and Rb atoms (Tab. S1 in SM). For the detection of the intermediate complex, a variable wavelength of 285 - 356 nm is used. To avoid any space-charge effects, the laser power is always chosen to ensure at most one ion per UV pulse is generated. The ODT is switched off for a variable time during and before the ionization pulse to eliminate its

role in the chemical reaction, the lifetime of the intermediate collisional complex, and the photo-ionization process. We repeat this detection procedure at 1 kHz for the reactant and product detection (see timing diagram in Fig. S1 of supplementary material (SM)), and at 7 kHz for the intermediate complex detection (see inset of Fig. 4(d)). The mass, and therefore species, of each detected ion can be inferred from its time-of-flight (TOF), whereas the momentum of the ion is mapped into its location on the VMI image [32].

To demonstrate the ionization detection capability in our ultracold molecular apparatus and to gain information beyond absorption imaging, we first probe the trapped KRb molecules in the ODT. The result is shown in Fig. 2(c) & 2(d). As expected, the dominant signal is  $\text{KRb}^+$ . The VMI image for the  $\text{KRb}^+$  signal has a width limited by the detector resolution, consistent with the negligible kinetic energy in the ultracold regime. Measurable amounts of  $\text{Rb}^+$  and  $\text{K}^+$  were also detected. The VMI images for  $\text{K}^+$  and  $\text{Rb}^+$  both show two distinct components: an isotropic central peak and an anisotropic ring. The ions forming the central peak originate from residual ultracold atoms from the molecule creation process after the cleanup pulses. Based on the known ionization cross sections and estimated ion detection efficiencies (Tab. S1 in SM), we put an upper bound of 250 atoms of each species in the trap. These populations are small compared to KRb, ensuring that the dominant reaction in the subsequent study is the desired bimolecular reaction. We note that this sensitive ionization detection allows us to quantify the small number of residual atoms in the ODT, and that these atoms are not seen using absorption imaging. To analyze the ions forming the ring pattern, we extract the kinetic energy release (KER) from the diameter of the ring to obtain a KER of  $8.3 \times 10^3 \text{ cm}^{-1}$ . We compare this KER to the calculated molecular potentials of KRb and  $\text{KRb}^+$  [33] and identify a two-photon dissociative ionization pathway that contributes to this atomic ion signal (Fig. S3 in SM).

After KRb molecules are created, the bimolecular reaction occurs immediately and continuously with a measured decay rate coefficient of  $7.6 \times 10^{-12} \text{ cm}^3/\text{s}$  until the reactants are depleted (Fig. 1 inset), consistent with previous studies [5]. To probe the products of the bimolecular reaction while reducing the perturbation to the reactants during ionization, we shape our ionization beam into a “hollow-bottle” such that the laser intensity is concentrated in a ring outside of the ODT while keeping the reactants in the “dark” with a measured intensity contrast between the peak and center of the beam of 500 [32]. The profile of this beam is illustrated in Fig. 3(b). To further reduce the hollow volume for higher efficiency ionization, we cross two hollow-bottle beams at a 40-degree angle centered on the ODT [32].

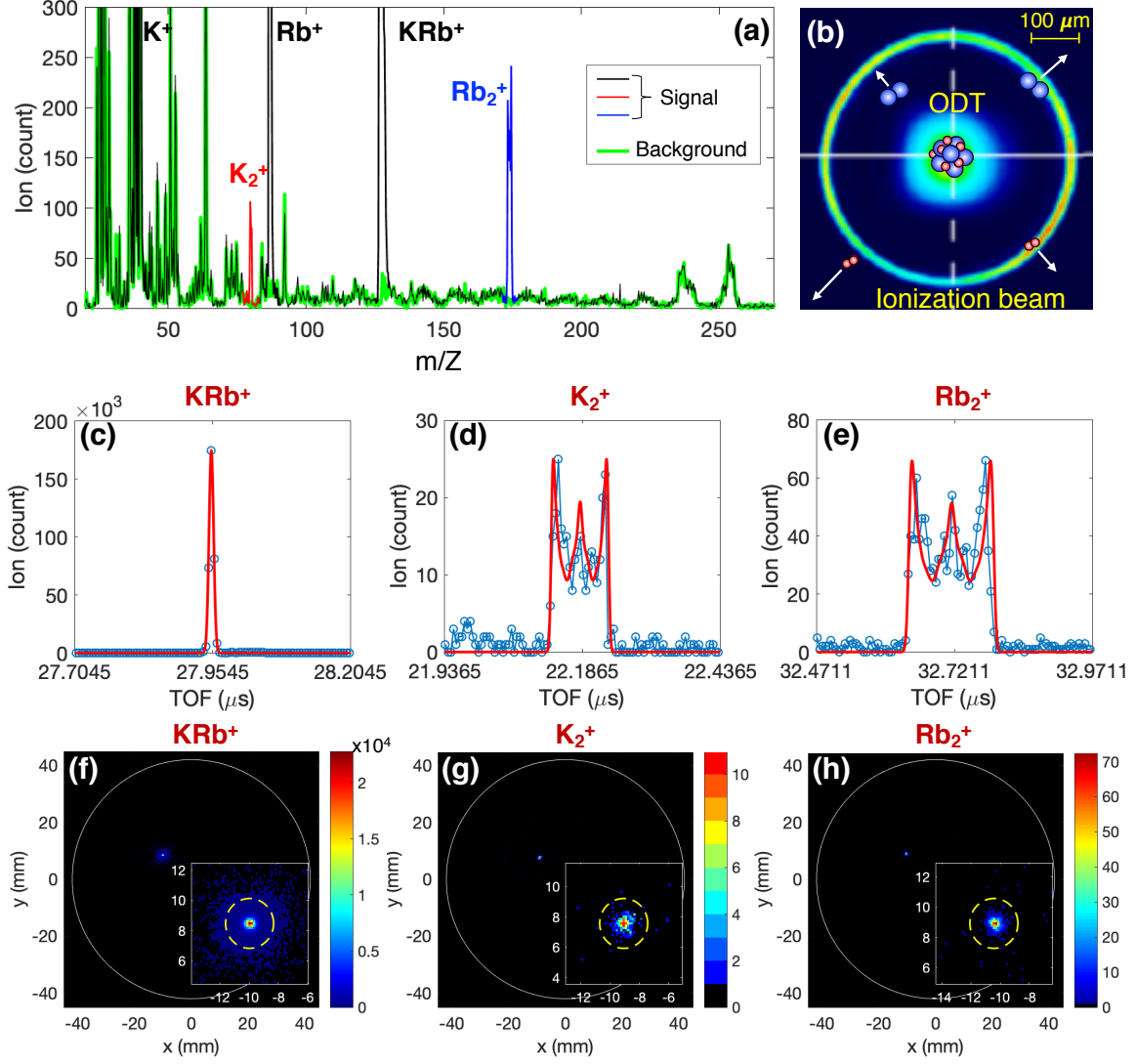


FIG. 3. **Identification of the reaction products.** (a) The mass spectrum of the reaction products ionized by 285 nm UV laser pulses. The color-coded ion signals correspond to species associated with the reaction of two KRb molecules compared to the ionization background (the green trace). (b) Geometries of the relevant beams with schematic representations of the reactants and products superimposed. The Gaussian beam spot in the center is the ODT and the ring surrounding it is the ionization beam. (c-e) The TOF data for  $KRb^+$ ,  $K_2^+$ , and  $Rb_2^+$  ions, respectively. The red curve in (c) is a simulated TOF lineshape for the ions generated in the center, while those in (d) and (e) are simulated TOF lineshape for the ions generated in the ring. (f-h) The momentum distributions of the  $KRb^+$ ,  $K_2^+$ , and  $Rb_2^+$  ions, respectively. The white solid circles represent the active area of the detector. The yellow dashed circles represent the momenta corresponding to  $10.4 \text{ cm}^{-1}$  of kinetic energy.

To observe the bimolecular reaction without the possible influence of the ODT light, we shut off the ODT for  $170 \mu s$  prior to each ionization pulse. This precludes any role of the ODT in the formation of all but those products with kinetic energy less than  $0.0127 \text{ cm}^{-1}$  [34].

The TOF mass spectrometry is shown in Fig. 3(a). The dominant peaks are again  $K^+$ ,

$\text{Rb}^+$ , and  $\text{KRb}^+$ , primarily from photo-ionization of trapped  $\text{KRb}$  molecules. Aside from these dominant peaks, we can clearly identify ions corresponding to the masses of  $\text{K}_2^+$ ,  $\text{Rb}_2^+$ . All peaks aside from these five species appear with comparable intensities in a background spectrum (green trace) taken in the absence of ultracold atoms and molecules.

We postulate that  $\text{K}_2^+$  and  $\text{Rb}_2^+$  come from direct ionization of reaction products,  $\text{K}_2$  and  $\text{Rb}_2$  (Fig. 1). To support such an assignment, we draw evidence from the TOF lineshapes and the VMI images. The TOF lineshapes characterize the spatial origin of the ions in the ionization beam. The  $\text{KRb}^+$  lineshape (Fig. 3(c)) is sharp and described well by the simulated lineshape for ions that come from the central part of the hollow ionization beams, which coincides with the position of the ODT.  $\text{K}_2^+$  and  $\text{Rb}_2^+$  share similar TOF lineshapes, as shown in Figs. 3(d) & 3(e). This lineshape is much wider than the  $\text{KRb}^+$  lineshape. The simulated lineshape (with only total amplitude as a free parameter, see SM) based on the beam geometry for particles ionized by the ring portion of the hollow ionization beams matches well to the data, which supports the assignment that they are from reaction products escaping the central  $\text{KRb}$  cloud. We also rule out the role of ion-neutral reactions due to their negligible estimated rates (Sec. S4 in SM).

In addition to the mass spectrometry of the  $\text{K}_2^+$  and  $\text{Rb}_2^+$  ions, we simultaneously record the momentum distribution of the  $\text{K}_2^+$  and  $\text{Rb}_2^+$  ions with VMI shown in Figs. 3(g) & 3(h). To characterize the radius of the distribution, we perform Bayesian fits to the images, assuming a circular Gaussian density on a flat background with uninformative priors. The radius of  $\text{K}_2^+$  ( $\text{Rb}_2^+$ ) corresponds to a kinetic energy of  $0.59 \text{ cm}^{-1}$  ( $0.29 \text{ cm}^{-1}$ ), well above the MCP resolution of  $0.02 \text{ cm}^{-1}$ . The ionization process of  $\text{K}_2$  ( $\text{Rb}_2$ ) would impart the resulting ion a photon recoil energy of  $0.0159 \text{ cm}^{-1}$  ( $0.0112 \text{ cm}^{-1}$ ), too small to significantly impact the momentum distribution of the ions. Therefore, the measured  $\text{K}_2^+$  and  $\text{Rb}_2^+$  kinetic energies closely resemble the kinetic energy released from the reaction. Both measured kinetic energies are smaller than the exothermicity,  $10.4 \text{ cm}^{-1}$ , of the bimolecular  $\text{KRb}$  reaction. Further, their kinetic energy ratio,  $0.49 \pm 0.06$ , is consistent with the expected ratio, 0.46, originating from two different mass products flying apart with zero center-of-mass momentum. This provides further evidence that supports the identification of  $\text{K}_2^+$  and  $\text{Rb}_2^+$  ions as arising from ionization of the products of the  $\text{KRb} + \text{KRb}$  chemical reaction.

Next, we focus on the transient intermediate collision complex,  $\text{K}_2\text{Rb}_2^*$ . In order to observe the complexes which by conservation of momentum should only exist in the vicinity of the reactants, we shape the UV ionization beam into a Gaussian beam profile. After data



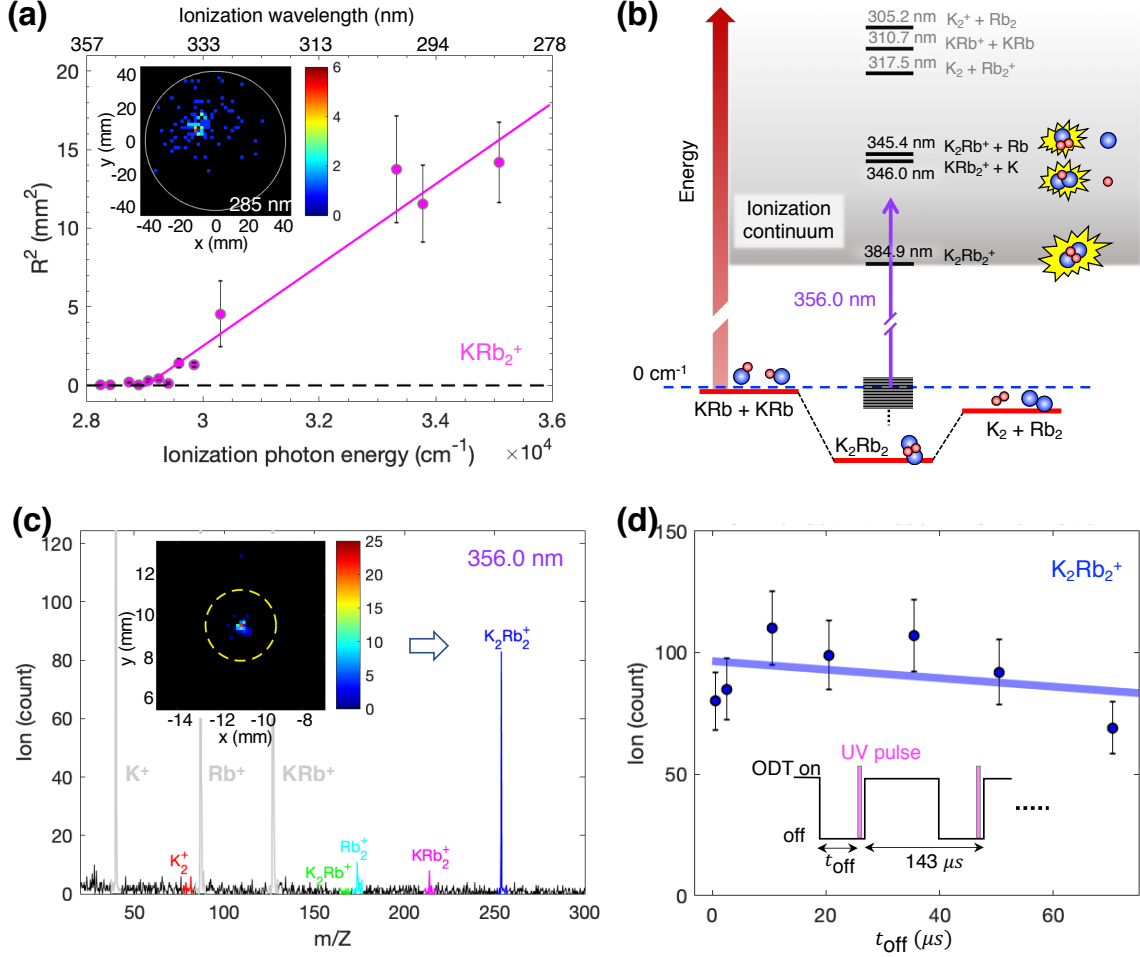


FIG. 4. **Direct detection of the intermediate complex  $K_2Rb_2^+$ .** (a) (Inset) The VMI image of detected  $K_2Rb_2^+$  ions (using an ionization laser wavelength of 285 nm). For each wavelength,  $R^2$  is extracted from such an image, where  $R$  is the Gaussian width of the ion spatial distribution, and  $R^2$  is proportional to the KER. The measured KER of  $K_2Rb_2^+$  ions is plotted versus the ionization photon energy. The solid line is a linear fit to the data above  $2.9 \times 10^4$  cm<sup>-1</sup>, from which an experimental dissociative ionization threshold wavelength of  $345 \pm 4$  nm is determined. (b) Calculated threshold wavelengths of the direct photo-ionization and dissociative ionization of the intermediate complex. The energies for the dissociative ionization thresholds are those corresponding to the equilibrium geometry of the ionic complex (Tab. S1 in SM) and are therefore lower bounds on the ionization energy. (c) TOF mass spectrum produced using an ionization laser wavelength of 356 nm. (Inset) The corresponding VMI image of the detected  $K_2Rb_2^+$  ions. The yellow dashed circle corresponds to  $10.4$  cm<sup>-1</sup>. (d)  $K_2Rb_2^+$  counts are plotted against  $t_{off}$ , where  $t_{off}$  denotes the length of ODT off time before UV photo-ionization. Error bars include shot noise and 10% molecule number fluctuations. A linear fit (blue line) determines a slope of  $-0.2 \pm 0.2$ , consistent with zero.

accumulation, we observe signals consistent with the masses of  $K_2Rb^+$  and  $KRb_2^+$  (Fig. S2 in SM). Based on their VMI images, which show large kinetic energies (Fig. 4(a) inset), we hypothesize that these ions are from dissociative ionization of  $K_2Rb_2^+$ . To substantiate this idea, we vary the wavelength of the ionization beam in order to determine the relationship

between the kinetic energy of the triatomic ions and the energy of the photon. In Fig. 4(a), we find that the characteristic kinetic energy associated with the  $\text{KRb}_2^+$  ion decreases as the ionization energy decreases. The ionization energy where the kinetic energy becomes zero (at  $345 \pm 4$  nm) agrees with our theoretical predictions ( $346 \pm 2$  nm) of the dissociative ionization threshold for the transient intermediate,  $\text{K}_2\text{Rb}_2^* + h\nu \rightarrow \text{KRb}_2^+ + \text{K}(4s) + e^-$ .

These theoretical calculations of ionization threshold energies of diatomic, triatomic, and tetratomic K- and Rb-containing molecules (shown in Fig. 4(b)) are based on the same methodology as in Ref. [35] and references therein. Briefly, each alkali-metal atom is modeled as a one-electron system in the field of an ionic core ( $\text{K}^+$  or  $\text{Rb}^+$ ). We use a semi-empirical effective core potential plus a core polarization potential to represent the correlation between the valence electron and the core electrons [32]. The  $\text{K}_2\text{Rb}^+$  and  $\text{KRb}_2^+$  triatomic ions are modeled as two-valence-electron systems, and the  $\text{K}_2\text{Rb}_2^+$  ion as a three-valence-electron molecule. In the framework of such a simplification, the ground-state potential energy surface (PES) can be obtained with a good accuracy via the diagonalization of the full electronic Hamiltonian (i.e. full configuration interaction) expressed on a large Gaussian basis set. Note that for all molecular and atomic species, the energies are computed with respect to the same origin, namely the energy of the four cores ( $\text{K}^+ + \text{K}^+ + \text{Rb}^+ + \text{Rb}^+$ ). This allows for the determination of transition energies between different species.

To directly observe the transient intermediate complex  $\text{K}_2\text{Rb}_2^*$ , we tune the wavelength of our ionization laser to 356 nm, with energy well below the lowest dissociative ionization channel. Figure 4(c) displays a mass spectrum obtained with ionization at 356 nm, and a strong signal of  $\text{K}_2\text{Rb}_2^+$  is detected. Although we have not yet directly measured the lifetime of the complex due to the technical challenges of precisely establishing a zero of time, the signal strength of our direct observation puts an estimate of a lifetime of 350 ns (or 3  $\mu\text{s}$ ), assuming the ionization cross-section of the  $\text{K}_2\text{Rb}_2$  intermediate complex is 10 Mb (or 1 Mb). This cross-section has not been reported in the literature. We emphasize that the ionization process transforms the transient intermediate into a bound molecular ion which can survive its flight to the MCP.

We further clarify the origin of the observed intermediate complexes, which has been the subject of previous debate [11, 23]. First, the long-lived transient complex could potentially collide with another particle, causing the prior's decay into a deeply-bound molecule and leading to the conversion of its internal energy into a large, observable KER [23, 24]. In contrast, we observe a detector resolution-limited small momentum distribution of the  $\text{K}_2\text{Rb}_2^+$

ions (Fig. 4(c) inset), consistent with the zero-momentum transient intermediate.

Second, because the reactants are trapped in the ODT, a light-assisted process could be a competing, confounding factor, as suggested by Ref. [11]. To examine the role of ODT, we have varied the length of time that the ODT is switched off prior to ionization, from 1  $\mu$ s to 70  $\mu$ s. If the ODT contributes to the formation of deeply-bound  $\text{K}_2\text{Rb}_2$  molecules, which have no radiative decay pathway and only potentially leave the probed volume on a millisecond time scale if they are untrapped, the  $\text{K}_2\text{Rb}_2$  would steadily build up concentration in the presence of the ODT. As a result, the concentration of  $\text{K}_2\text{Rb}_2$  should decrease monotonically as we increase the ODT off duration. Instead, we find the yield of  $\text{K}_2\text{Rb}_2^+$  ions has no monotonic trend with the ODT off duration (see Fig. 4(d)). This result is evidence that the intermediates we observe are formed upon collision of two KRb molecules, with no measurable effect from the ODT, on or off.

The direct observation of  $2 \text{KRb} \rightarrow \text{K}_2\text{Rb}_2^* \rightarrow \text{K}_2 + \text{Rb}_2$  opens numerous possibilities of exploring the detailed role of quantum mechanics in ultracold chemical reaction dynamics by measuring the lifetime of the intermediate complex [23, 24], testing the transition from quantum to semiclassical reactions [36], and resolving the quantum states of the reaction products [37] and the intermediate.

Acknowledgment: We thank T. Rosenband and J. Ye for discussion, K. Liu for introducing us to the VMI techniques, T. Pfau, E. Narevicius and M. Greiner for discussions on apparatus design, J. Doyle for loaning laser equipment, and W. Stwalley, P. Gould and the late E. Eyler for sharing KRb spectroscopy literature. The  $^{40}\text{K}$  isotope used in this research was supplied by the United States Department of Energy Office of Science by the Isotope Program in the Office of Nuclear Physics. Funding: This work is supported by the DOE Young Investigator Program, the David and Lucile Packard Foundation, and the NSF through Harvard-MIT CUA.

- 
- [1] A. B. Henson, S. Gersten, Y. Shagam, J. Narevicius, and E. Narevicius, *Science* **338**, 234 (2012).
  - [2] H. Yang, D.-C. Zhang, L. Liu, Y.-X. Liu, J. Nan, B. Zhao, and J.-W. Pan, *Science* **363**, 261 (2019).
  - [3] P. Puri, M. Mills, C. Schneider, I. Simbotin, J. A. Montgomery, R. Côté, A. G. Suits, and E. R. Hudson, *Science* **357**, 1370 (2017).
  - [4] D. K. Hoffmann, T. Paintner, W. Limmer, D. S. Petrov, and J. H. Denschlag, *Nature communications* **9**, 5244 (2018).
  - [5] S. Ospelkaus, K.-K. Ni, D. Wang, M. De Miranda, B. Neyenhuis, G. Quémener, P. Julienne, J. Bohn, D. Jin, and J. Ye, *Science* **327**, 853 (2010).

- [6] A. Kilaj, H. Gao, D. Rösch, U. Rivero, J. Küpper, and S. Willitsch, *Nature communications* **9** (2018).
- [7] L. De Marco, G. Valtolina, K. Matsuda, W. G. Tobias, J. P. Covey, and J. Ye, *Science* **363**, 853 (2019).
- [8] N. Balakrishnan, *The Journal of Chemical Physics* **145**, 150901 (2016).
- [9] X. Ye, M. Guo, M. L. González-Martínez, G. Quémener, and D. Wang, *Science advances* **4**, eaag0083 (2018).
- [10] P. D. Gregory, M. D. Frye, J. A. Blackmore, E. M. Bridge, R. Sawant, J. M. Hutson, and S. L. Cornish, *Nature communications* **10**, 3104 (2019).
- [11] A. Christianen, M. W. Zwierlein, G. C. Groenenboom, and T. Karman, *arXiv:1905.06846* (2019).
- [12] S. Bauer, *Annual Review of Physical Chemistry* **30**, 271 (1979).
- [13] W. Miller, S. Safron, and D. Herschbach, *The Journal of Chemical Physics* **56**, 3581 (1972).
- [14] A. H. Zewail, *The Journal of Physical Chemistry A* **104**, 5660 (2000).
- [15] M. Gruebele, I. Sims, E. Potter, and A. Zewail, *The Journal of chemical physics* **95**, 7763 (1991).
- [16] I. Sims, M. Gruebele, E. Potter, and A. Zewail, *The Journal of chemical physics* **97**, 4127 (1992).
- [17] J. C. Polanyi and A. H. Zewail, *Accounts of Chemical Research* **28**, 119 (1995).
- [18] C. C. Womack, M.-A. Martin-Drumel, G. G. Brown, R. W. Field, and M. C. McCarthy, *Science advances* **1**, e1400105 (2015).
- [19] B. J. Bjork, T. Q. Bui, O. H. Heckl, P. B. Changala, B. Spaun, P. Heu, D. Follman, C. Deutsch, G. D. Cole, M. Aspelmeyer, *et al.*, *Science* **354**, 444 (2016).
- [20] T. Q. Bui, B. J. Bjork, P. B. Changala, T. L. Nguyen, J. F. Stanton, M. Okumura, and J. Ye, *Science advances* **4**, eaag4777 (2018).
- [21] E. Garand, J. Zhou, D. E. Manolopoulos, M. H. Alexander, and D. M. Neumark, *Science* **319**, 72 (2008).
- [22] Y.-T. Su, Y.-H. Huang, H. A. Witek, and Y.-P. Lee, *Science* **340**, 174 (2013).
- [23] M. Mayle, G. Quémener, B. P. Ruzic, and J. L. Bohn, *Physical Review A* **87**, 012709 (2013).
- [24] A. Christianen, T. Karman, and G. C. Groenenboom, *arXiv:1905.06691* (2019).
- [25] D. J. Nesbitt, *Chemical Reviews* **112**, 5062 (2012).
- [26] K.-K. Ni, S. Ospelkaus, M. De Miranda, A. Pe’Er, B. Neyenhuis, J. Zirbel, S. Kotochigova, P. Julienne, D. Jin, and J. Ye, *Science* **322**, 231 (2008).
- [27] S. Falke, I. Sherstov, E. Tiemann, and C. Lisdat, *The Journal of chemical physics* **125**, 224303 (2006).
- [28] C. Amiot, *The Journal of Chemical Physics* **93**, 8591 (1990).
- [29] J. N. Byrd, J. A. Montgomery Jr, and R. Côté, *Physical Review A* **82**, 010502 (2010).
- [30] T. D. Cumby, R. A. Shewmon, M.-G. Hu, J. D. Perreault, and D. S. Jin, *Physical Review A* **87**, 012703 (2013).
- [31] A. T. Eppink and D. H. Parker, *Review of Scientific Instruments* **68**, 3477 (1997).
- [32] See details in the supplementary material.
- [33] M. Korek, G. Younes, and A. Allouche, *International journal of quantum chemistry* **92**, 376 (2003).
- [34]  $170\ \mu\text{s}$  is the time it will take for a  $\text{Rb}_2$  molecule with kinetic energy of  $0.0127\ \text{cm}^{-1}$  to travel from the center of the KRb cloud to the ionization ring that has a diameter of 0.45 mm.
- [35] R. Vexiau, D. Borsalino, M. Lepers, A. Orbán, M. Aymar, O. Dulieu, and N. Bouloufa-Maafa, *International Reviews in Physical Chemistry* **36**, 709 (2017).
- [36] B. Gao, *Physical Review Letters* **105**, 263203 (2010).
- [37] J. Croft, C. Makrides, M. Li, A. Petrov, B. Kendrick, N. Balakrishnan, and S. Kotochigova, *Nature communications* **8**, 15897 (2017).

# Supplementary Material for Direct Observation of Ultracold Bimolecular Reactions

M.-G. Hu,<sup>1,2,3,\*</sup> Y. Liu,<sup>2,1,3,\*</sup> D. D. Grimes,<sup>1,2,3</sup> Y.-W. Lin,<sup>1,2,3</sup>  
A. H. Gheorghe,<sup>2</sup> R. Vexiau,<sup>4</sup> N. Boulufa-Maafa,<sup>4</sup> O. Dulieu,<sup>4</sup> and K.-K. Ni<sup>1,2,3,†</sup>

<sup>1</sup>*Department of Chemistry and Chemical Biology,*

*Harvard University, Cambridge, Massachusetts, 02138, USA.*

<sup>2</sup>*Department of Physics, Harvard University, Cambridge, Massachusetts, 02138, USA.*

<sup>3</sup>*Harvard-MIT Center for Ultracold Atoms, Cambridge, Massachusetts, 02138, USA.*

<sup>4</sup>*Laboratoire Aimé Cotton, CNRS, Université Paris-Sud,*

*ENS Paris-Saclay, Université Paris-Saclay, 9145 Orsay cedex, France*

## S1. PHOTO-IONIZATION AND VELOCITY-MAP IMAGING OF IONS

Our photo-ionization laser system is a frequency-doubled, broadly tunable pulsed dye laser (LIOP-TEC/LiopStar-HQ) pumped by a pulsed Nd:YAG laser (EdgeWave BX80). It has a variable repetition rate of up to 10 kHz, a pulse duration of 7 ns, a spectral width of 0.06 cm<sup>-1</sup>, and a tuning range of 220 - 400 nm (after frequency-doubling by a BBO3 crystal). Once the ground state KRb molecules are created in the ODT, they immediately begin to react with each other. In order to perform photo-ionization detection on the reaction products, we follow the sequence of events shown in Fig. S1. The sequence for detecting the intermediate is the same except for the repetition rate and ODT switch off time (see inset of Fig. 4(d)). To distinguish signal from background noise, we take two TOF mass spectra in succession for all of the experiments carried out in this study. The ODT is switched off for 400 ms between the recordings of the two spectra to ensure that all particles in the ODT are dropped out before we take the background spectrum. An example set of spectra is shown in Fig. S2, where ion signals are recorded as the reaction is probed by a 285 nm UV laser with a Gaussian beam profile. By comparing the spectra in Fig. S2(a) and Fig. S2(b), we can clearly distinguish the signal mass peaks from the background.

We designed and built Velocity Map Imaging (VMI) ion optics in order to project the momentum/kinetic energy distribution of the photo-ionized neutrals into a spatial distribution

\* These two authors contributed equally.

† To whom correspondence should be addressed. E-mail: ni@chemistry.harvard.edu

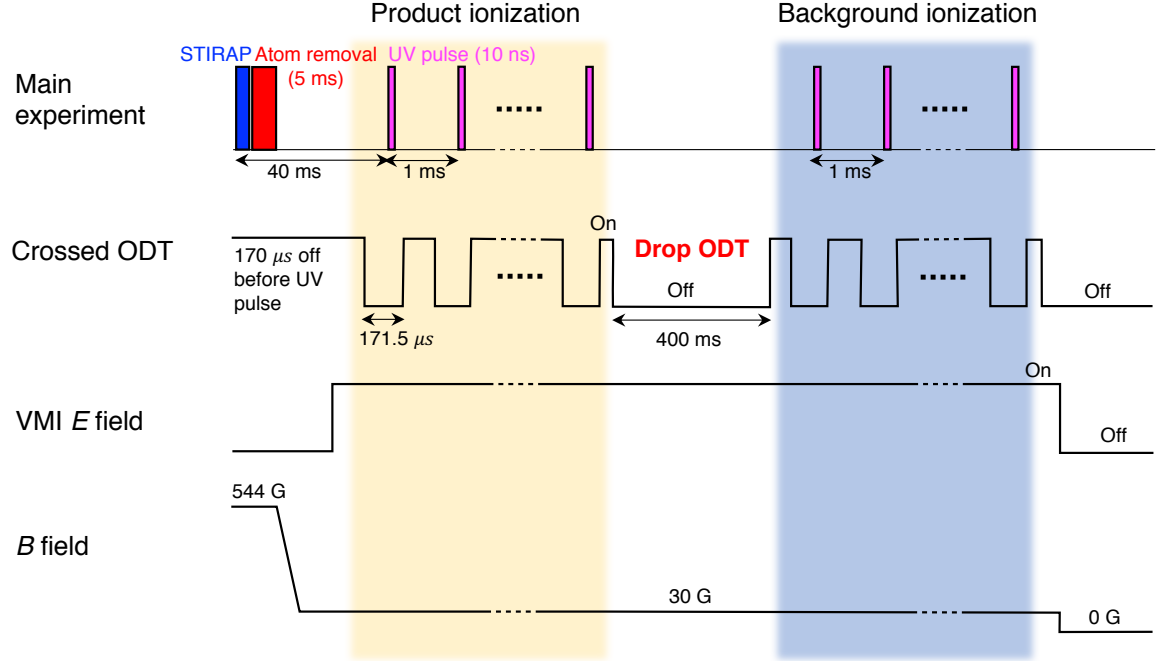


FIG. S1. **Timing diagram for photo-ionization detection of an ultracold chemical reaction.** When VMI electrodes are on, it generates a 180 V/cm electric field at the location of the ODT. The ODT is turned off for 400 ms between the product ionization stage and the background ionization stage to ensure that all particles inside the ODT drop out under gravity.

that can be detected by a position sensitive delay-line MCP (RoentDek/DLD80). The MCP has an active detection area of  $\varnothing$  80 mm, a spatial resolution of 0.08 mm, and a temporal resolution of 20 ns. A VMI setup consists of three main electrode plates: a repeller plate, an extractor plate, and a ground plate, with the geometries and voltages of these electrodes chosen to form the VMI configuration [1]. Before ionization, a small volume of neutral reaction products sits between the repeller and the extractor. After ionization, charged species are accelerated towards the ion detector along the TOF axis while they ballistically expand away from that axis at a rate determined by their transverse velocities. The spatial distribution of ions on the detector associated with each species forms its VMI image. The transverse kinetic energy ( $KE$ ) of each ion is mapped to its radial distance  $R$  from the center of the image according to the relation  $R = A \cdot \sqrt{KE/V_R}$ , where  $V_R$  is the repeller voltage and  $A = 16.44 \text{ mm}/\sqrt{\text{cm}^{-1}/\text{V}}$ .

For chemical reactions that occur at less than 1  $\mu\text{K}$ , the kinetic energy of the reactants is negligibly small. Therefore, the momentum of the ions enables us to determine if the ions are

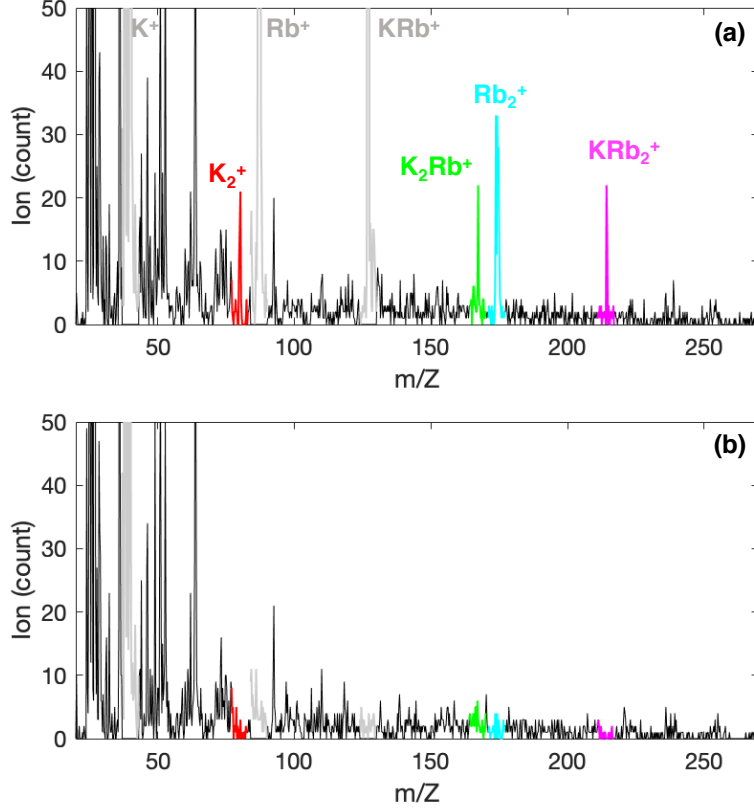


FIG. S2. Mass spectra recorded as the reaction is probed by a 285 nm UV laser with a Gaussian beam profile. (a) Signal spectrum. (b) Background spectrum.

generated via direct or dissociative photo-ionization. The former only detaches an electron, and thus causes no measurable change on kinetic energy of ions. The latter involves breaking chemical bonds and generally involves a significant increase of ion kinetic energy. As shown in Fig. S3 (a-b), from the VMI signals of both  $K^+$  and  $Rb^+$  ions, we observe two features: an isotropic central peak and an anisotropic ring. Because the ions from the central peak have a very small kinetic energy, we identify them as produced via single-photon ionization of the ultracold K and Rb atoms left in the ODT. This identification is further confirmed by the observation that these small features disappear when we tune the UV photon energy below the atomic ionization thresholds of K and Rb. For ions that form the ring, we can determine the kinetic energy release (KER) from the radius of the ring, and the energy matches well to the dissociative ionization potentials of KRb (see Fig. S3(c-d)). Therefore, we identify these ions as originating from dissociative ionization of the ultracold KRb molecules.

In Tab. S1, we summarize the ionization energy thresholds of relevant molecular species

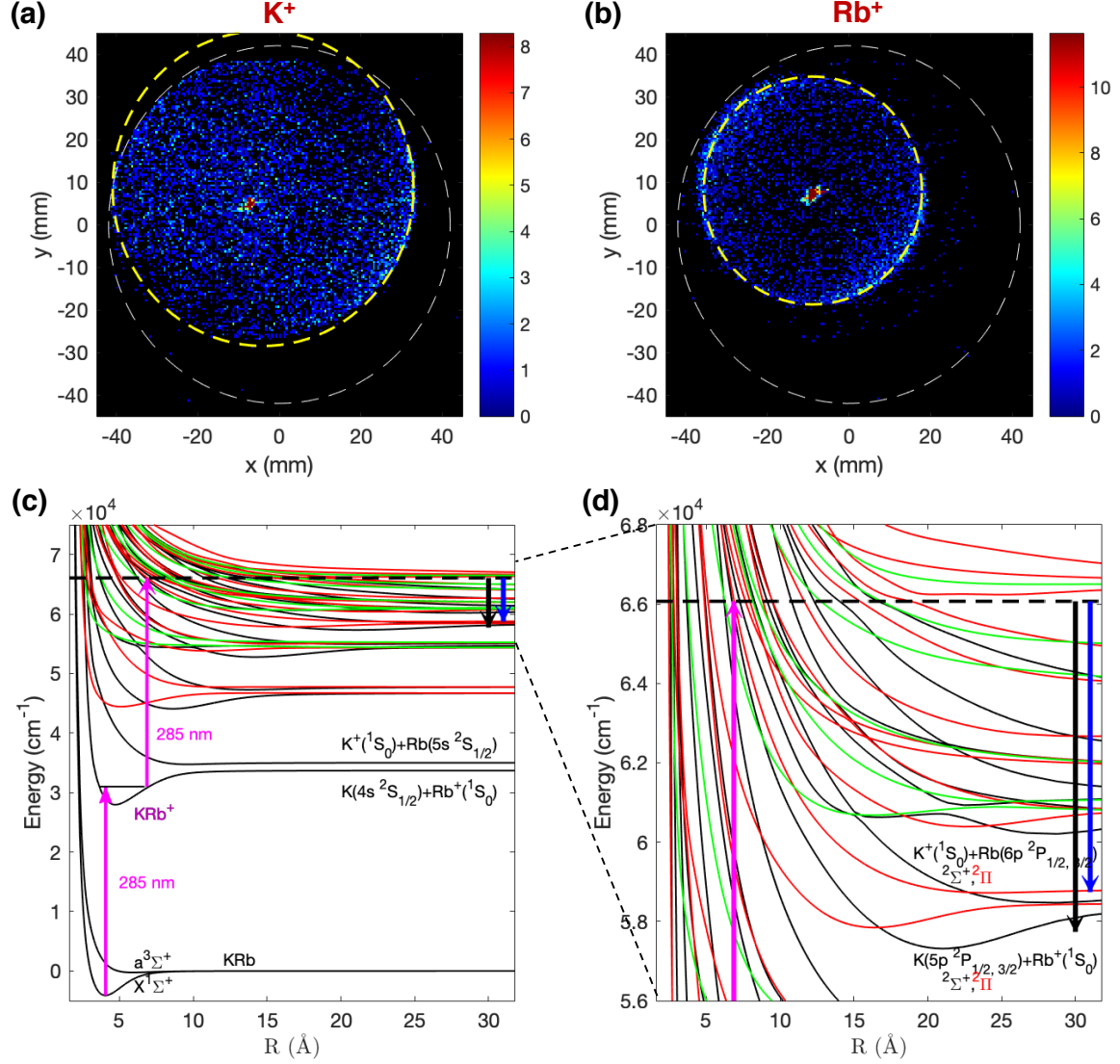


FIG. S3. **Photo-ionization of GS KRb molecules.** (a-b) Measured VMI signals of  $K^+$  and  $Rb^+$  ions at 285 nm and  $V_R = 1000$  V. The white dashed circles represent the detector active area. The yellow dashed circles correspond to the momenta of the  $K^+$  and  $Rb^+$  ions acquired during the dissociative ionization of ground state KRb molecules. The radius of the yellow circle for the  $K^+$  ( $Rb^+$ ) ions is 37 mm (27 mm) corresponding to KER of  $0.73 \times 10^4 \text{ cm}^{-1}$  ( $0.83 \times 10^4 \text{ cm}^{-1}$ ). (c-d) Energy diagram for KRb and  $KRb^+$  molecules. The potential energies of the electronic states of molecular  $KRb^+$  ions are taken from Ref. [2]. The magenta arrows represent the photon energy of the ionization laser.  $KRb^+$  ions are generated via single-photon ionization. In addition,  $K^+$  and  $Rb^+$  ions are generated via two-photon dissociative ionization, during which the released energy is distributed between  $Rb^+$  ( $Rb$ ) and  $K$  ( $K^+$ ) according to their mass ratio. The measured KER,  $0.73 \times 10^4 \text{ cm}^{-1}$ , from the VMI signal of  $K^+$  ions in (a) is drawn as the blue arrow above, which matches the energy of the dissociative ionization channels,  $K^+(^1S_0) + Rb(6p \ ^2P_{1/2,3/2})$ . The measured KER,  $0.83 \times 10^4 \text{ cm}^{-1}$ , from the VMI signal of  $Rb^+$  ions in (b) is drawn as the black arrow above, which matches the energy of the dissociative ionization channels,  $K(5p \ ^2P_{1/2,3/2}) + Rb^+(^1S_0)$ .



to this work. Experimentally measured thresholds are available for the atomic and diatomic species from literature. The triatomic and tetratomic thresholds are derived from the differences between the energies of their respective ion and neutral rovibronic ground states. The neutral triatomic and tetratomic energies are calculated in Ref. [3]. The ionic triatomic and tetratomic energies are calculated in this work using the following methods. The molecular species are described in Jacobi coordinates. We did not derive here the full PES of their electronic ground state. Instead, inspired by previous results on metallic clusters [4, 5], we first looked at each potential local minimum of the molecular species:  $C_{2v}$  and linear for the triatomic ion, diamond, T-shaped and linear for the tetratomic ion, with each possible arrangement of the individual atoms. We computed the potential energy on a sparse grid (steps of 0.3 a.u. in each radial distance, the angles being fixed by the selected geometry), and compared the values for the different geometries. Once the global minimum is found a more accurate calculation is made (steps of 0.02 a.u.) to pinpoint the potential energy at the equilibrium geometry.

## S2. IONIZATION BEAM GEOMETRY

The output of the pulsed UV laser is shaped into a beam with a  $\varnothing$  3 mm. To detect the reactants or intermediate complex we shrink down the beam to create a  $\varnothing$  300  $\mu\text{m}$  Gaussian profile at the molecule location. To detect the products we generate hollow-bottle beams following the optical system design from Ref. [12]. Each hollow beam has a  $\varnothing$  0.45 mm ring-shaped profile centered around the KRb cloud, with a Gaussian width of 5.9  $\mu\text{m}$ . We generate two such hollow beams and cross them at a  $40^\circ$  angle centered on the ODT to maximize the capture solid angle of the reaction products. Due to a combination of limited numerical aperture, finite sharpness of the tip of the axicon, and the spatial mode of the input beam, the center of each hollow beam is not perfectly dark. We estimate the intensity at the center of the hollow beam to be  $\sim 0.2\%$  of its peak intensity. This explains the presence of in-trap species (K, Rb, and KRb) in our mass spectrum (Fig. 3a) acquired with the crossed hollow beam.

TABLE S1. Ionization information for all relevant species in the experiment. We define the photo-ionization threshold here as the energy required to excite from the ground rovibronic state of the neutral to the ground rovibronic state of the ion. The photo-ionization cross section is shown for excitation at 285 nm.

Species	Photo-ionization threshold (nm)	Photo-ionization cross section $\sigma$ (Mb <sup>a</sup> )	MCP detector efficiency <sup>b</sup>
K	285.6 (Ref. [7])	0.01 (Ref. [7])	0.394
Rb	296.8 (Ref. [8])	0.049 (Ref. [8])	0.355
K <sub>2</sub>	305.1 <sup>c</sup> (Ref. [9])	$0.50 \pm 0.25$ (Ref. [10])	0.360
Rb <sub>2</sub>	317 <sup>c</sup> (Ref. [8])	$0.58 \pm 0.26$ (Ref. [8, 10])	0.310
KRb	310.0 – 320.3 <sup>c</sup> (Ref. [11])		0.331
K <sub>2</sub> Rb	374.9 <sup>d</sup> (this work)		0.313
KRb <sub>2</sub>	377.6 <sup>d</sup> (this work)		0.295
K <sub>2</sub> Rb <sub>2</sub>	347.65 <sup>e</sup> (this work)		0.282

<sup>a</sup> 1 Mb =  $10^{-18}$  cm<sup>2</sup>.

<sup>b</sup> Values are calculated using the empirical formula developed in Ref. [6] based on the ion's mass and kinetic energy. We take into account both the intrinsic efficiency of the channel plates (60% open-area-ratio) of our MCP and the 75% optical transmission of a mesh in front of the plates. The maximum detection efficiency, in the limit of light mass and high kinetic energy, is  $0.60 \times 0.75 = 0.45$ .

<sup>c</sup> It is calculated to be 305.2 nm for K<sub>2</sub>, 317.5 nm for Rb<sub>2</sub>, and 310.72 nm for KRb in this work.

<sup>d</sup> These values are calculated for the equilibrium geometries of the ionic complexes KRb<sub>2</sub><sup>+</sup> (*C*<sub>2v</sub>):  $R = 7.15$  a.u.,  $r_{\text{Rb}_2} = 8.88$  a.u.,  $\theta = 90^\circ$  and RbK<sub>2</sub><sup>+</sup> (*C*<sub>2v</sub>):  $R = 7.51$  a.u.,  $r_{\text{K}_2} = 8.08$  a.u.,  $\theta = 90^\circ$ . Here we use Jacobi coordinates:  $r$  is distance of the homonuclear pair and  $R$  is distance from the third partner to the center of the homonuclear pair. The threshold for K<sub>2</sub>Rb<sub>2</sub><sup>+</sup> +  $h\nu \rightarrow$  K<sub>2</sub>Rb<sup>+</sup> + Rb(5S) +  $e^-$  is 345.4 nm and the threshold for K<sub>2</sub>Rb<sub>2</sub><sup>+</sup> +  $h\nu \rightarrow$  KRb<sub>2</sub><sup>+</sup> + K(4S) +  $e^-$  is 346.0 nm.

<sup>e</sup> This value is calculated for the equilibrium geometry of the ionic complexes K<sub>2</sub>Rb<sub>2</sub><sup>+</sup> (T-shaped):  $R = 11.8$  a.u.,  $r_{\text{K}_2} = r_{\text{Rb}_2} = 8.5$  a.u.. Here  $R$  is distance between K<sub>2</sub> center and Rb<sub>2</sub> center. The threshold for K<sub>2</sub>Rb<sub>2</sub><sup>+</sup> +  $h\nu \rightarrow$  K<sub>2</sub>Rb<sub>2</sub><sup>+</sup> +  $e^-$  is 384.9 nm.

### S3. MODELING THE TIME-OF-FLIGHT LINESHAPES OF REACTION PRODUCTS

Species ionized in the ring of peak intensity of the hollow beam have a different TOF lineshape than species ionized in the weak center of the hollow beam. Ions that are generated closer to the MCP arrive later and those generated further from the MCP arrive earlier. This is because ions that are generated closer to the MCP experience less time in the accelerating electric fields and so have a lower velocity in the field-free drift region. In order to simulate a TOF distribution for ions generated in the ring, we determine the distance between where they are ionized and the MCP. In order to do this, we assume an isotropic distribution of exit velocity vectors from the ODT, and then determine where the product molecule associated with each velocity vector crosses the peak intensity of the ionization beam. We then use this position to determine the TOF associated with each velocity vector, and sum

over all exit velocity vectors to construct the total TOF lineshape. For the simulation, we use physical parameters of our system such as the radius of the hollow bottle beams, 0.45 mm, the intersection angle of the two hollow beams,  $40^\circ$ , and the details of the ion optics (plate voltages and distances from each other). The only fitting parameter in this model is the overall amplitude of the signal. Examples of this lineshape overlaid on data are shown in Figure 3(d) and 3(e). The center peak in the lineshape is due to product species that are ejected from the ODT with their velocity vectors primarily normal to the axis of the MCP, while the outer two peaks are due to product species that are ejected with their velocity vectors primarily toward or away from the MCP being ionized at roughly the same distance from the ODT in the direction of the MCP.

#### S4. ION-NEUTRAL COLLISIONS

The rate of ion-neutral collisions can be estimated by using a long-range capture model to determine the Langevin rate coefficient. The rate coefficient for ion-dipole collisions is [13]:

$$k_{\text{Ion-Dipole}}(T) = \frac{\mu_D q}{4} \left[ \frac{8\pi}{\mu} \right]^{\frac{1}{2}} (k_B T)^{-\frac{1}{2}} \frac{1}{4\pi\epsilon_0} \quad (\text{S.1})$$

where  $\mu_D$  is the dipole moment of the molecule,  $q$  is the charge of the ion,  $\mu$  is the reduced mass of the ion-dipole system, and  $T$  is the energy of the collision in units of Kelvin. A  $\text{KRb}^+$  ion generated in the center of the ODT has exited the trap (using the  $4\sigma$  width as the trap dimension) within 70 ns of being created. As the  $\text{KRb}^+$  ions are accelerated towards the MCP, their Langevin rate coefficients rapidly decrease as the kinetic energy of the ion increases. The average number of collisions that a  $\text{KRb}^+$  ion formed in the center of an ODT with a density of neutral KRB molecules of  $10^{12} \text{ cm}^{-3}$  experiences is  $2.5 \times 10^{-5}$ .

Ion-neutral collisions could be a potentially confounding factor in all of the experiments we describe in the main text. A collision between KRB and  $\text{KRb}^+$  is potentially reactive and can lead to the formation of diatomic, triatomic, or tetratomic ions of the same species as the ones we observe in the experiments. To place an upper bound on the number of ion-neutral reaction products generated in each experimental cycle, we estimate the number of  $\text{KRb}^+$  produced by the photo-ionization of KRB, calculate the number of ion-neutral collisions, and make the assumption that every such collision leads to the formation of a product ion. These estimates are compared to our measured number of ions per experimental cycle below.

Varying experimental conditions (repetition rate, ionization beam geometry, ionization laser power, ionization wavelength) between different experiments leads to differing amounts of  $\text{KRb}^+$  generated and therefore differing rates of ion-neutral collisions. The  $\text{K}_2$  and  $\text{Rb}_2$  product experiment (Fig. 3) has a maximum creation rate of product molecular ions via ion-neutral collisions of  $7.2 \times 10^{-3}$  per experimental cycle, compared to the observed values of 0.82  $\text{K}_2^+$  and 4.2  $\text{Rb}_2^+$  per experimental cycle. The dissociative ionization trimer experiment (Fig. 4(a)) has a maximum creation rate of trimer molecular ions via ion-neutral collisions of  $1.4 \times 10^{-3}$  per experimental cycle, compared to the observed values of 0.03 per experimental cycle for both  $\text{KRb}_2^+$  and  $\text{K}_2\text{Rb}^+$ . The transient intermediate complex experiment (Fig. 4(c)) has a maximum creation rate of tetramer molecular ions via ion-neutral collisions of  $1.0 \times 10^{-4}$  per experimental cycle, compared to the observed value of 1.2 per experimental cycle. Based on these comparisons, we conclude that ion-neutral reactions do not significantly contribute to the measured ion signals in any of our experiments.

- 
- [1] A. T. Eppink and D. H. Parker, Review of Scientific Instruments **68**, 3477 (1997).
  - [2] M. Korek, G. Younes, and A. Allouche, International journal of quantum chemistry **92**, 376 (2003).
  - [3] J. N. Byrd, J. A. Montgomery Jr, and R. Côté, Physical Review A **82**, 010502 (2010).
  - [4] A. Ray, Solid state communications **71**, 311 (1989).
  - [5] A. Ray and S. Berry, Journal of Physics B: Atomic, Molecular and Optical Physics **23**, 2365 (1990).
  - [6] M. Krems, J. Zirbel, M. Thomason, and R. D. DuBois, Review of Scientific Instruments **76**, 093305 (2005).
  - [7] R. Hudson and V. Carter, Physical Review **139**, A1426 (1965).
  - [8] H. Suemitsu and J. A. Samson, Physical Review A **28**, 2752 (1983).
  - [9] M. Broyer, J. Chevalere, G. Delacretaz, S. Martin, and L. Wöste, Chemical Physics Letters **99**, 206 (1983).
  - [10] D. Creek and G. Marr, Journal of Quantitative Spectroscopy and Radiative Transfer **8**, 1431 (1968).
  - [11] M. M. Kappes, M. Schaer, and E. Schumacher, The Journal of Physical Chemistry **89**, 1499 (1985).
  - [12] S. Kulin, S. Aubin, S. Christe, B. Peker, S. L. Rolston, and L. A. Orozco, Journal of Optics B: Quantum and Semiclassical Optics **3**, 353 (2001).
  - [13] D. Clary, Annual Review of Physical Chemistry **41**, 61 (1990).